Journal of Sound and Vibration (1996) **192**(4), 741–769

EIGENSOLUTIONS OF ANNULAR-LIKE ELASTIC DISKS WITH INTENTIONALLY REMOVED OR ADDED MATERIAL

H. VINAYAK AND R. SINGH

Acoustics & Dynamics Laboratory, Department of Mechanical Engineering, The Ohio State University, Columbus, OH 43210-1107, *U.S.A.*

(*Received* 25 *January* 1995, *and in final form* 23 *August* 1995)

Many examples of elastic, isotropic, stationary annular-like disks are studied analytically and experimentally for free–free and clamped–free boundary conditions. Natural frequencies and deformation shapes of the first few flexural modes including repeated roots are examined and tabulated. Disks with large circular holes or annular holes or annular slots within the disk body with a volume or mass ratio Γ of 5 to 15% are studied with particular emphasis on mode shapes as they deviate from the regular annular plate modes. Material removal cases via incisions or minor cuts at the disk rim, hub or within the body are not considered in this investigation. Material addition cases are simulated by thickening the outer rim or inner hub regions, for Γ values up to 60%. The final example considers a gear from a helicopter tail rotor gearbox; it has 8 holes and thick rim and hub. A bi-orthogonal polynomial-trigonometrical shape function series is proposed in the Ritz minimization scheme that employs both classical thin and Mindlin's thick plate theories. The effect of number of terms is evaluated by examining an expansion of the linearly independent basis function and by calculating an overall root mean square (rms) error associated with the prediction of a mode shape. The clamped inner edge is described by 4 alternate models and the impedance boundary condition described was found to be the most satisfactory. Predictions of the semi-analytical Ritz method closely match with measured eigensolutions and results yielded by finite element models. The Ritz method is especially attractive because of significant computational savings in addition to the ease with which it can be integrated within a component mode synthesis or multi-body dynamics framework for forced response or system design studies.

1. INTRODUCTION

Many practical machine elements and structural components such as circular cutters, gear bodies, compressor valves, clutches, flywheels, etc. resemble annular plates or disks. Holes, slots or grooves are often cut into the disk blank, within the body or at the rim, to achieve design or body performance criteria which may range from weight reduction to stress relief and noise control. Also, material may be added to the blank through ribs, rings, and concentrated weights to ensure adequate stiffness, rigidity, or balance. Deviations from the perfect annular geometry are sometimes significant and obviously related to the function or purpose of the component. It is of course understood that given the irregular geometry, one must adopt numerical methods (such as finite elements) or experimental approaches to investigate the resulting vibratory behavior and to conduct parametric studies. But, each analysis is usually carried out after the component has already been specified, designed or fabricated. Also, each design may appear to be problem or product specific. How are the dynamics of such annular-like disks described mathematically on a common basis? This

0022–460X/96/190741 + 29 $18.00/0

is accomplished in this article by proposing a semi-analytical method that addresses a family of dynamic design problems. Measured and computed eigensolutions of some typical annular-like disk concepts are also presented to aid the designer. The scope of the article is however restricted to the first few flexural modes and the resulting disk is assumed to be isotropic, homogeneous, and elastic.

There is a substantial body of literature on the eigensolutions of annular and circular plates as evident from the well known monograph by Leisse [1]. Beyond this, several publications have examined the effects of variable thickness, slots, holes, cut outs, and elastic inclusions on the dynamic response of plates or disks [1–5]. For instance, Lee [2] has analyzed a non-uniform annular plate and determined the fundamental frequencies by using the Rayleigh's method. Similar efforts have been made by Laura *et al*. for stepped plates [3]. Yu and Mote [4] have investigated the role of radial slots at the rim and clarified the distinction between split and repeated modes for both stationary and rotating circular plates. Shen and Mote [5] have extended the previous work by proposing a perturbation approach to the vibration analysis of finite solids containing small elastic imperfections; a circular plate with radial inclusions is the primary example of their work. Numerous articles on elastic imperfections, flaws, and cracks have appeared and a variety of analytical and numerical approaches have been employed; refer to Shen and Mote [5] for a detailed review of prior publications on this topic. Further discussion on shape functions and boundary conditions will be presented in later sections (3.3 and 5.1).

2. PROBLEM FORMULATIONS

Even though the plate vibration literature [1–24] appears to be rich, it is believed that the subject of this paper has yet to be addressed in sufficient depth. Accordingly, an annular blank is considered where large holes, slots, or attachments are introduced at the mechanical design stage and manufactured as such. Such changes in the blank structure are assumed to be clearly beyond the scope of theory governing small imperfections, incisions, or cracks [4, 5]. Specific objectives of the current article are as follows. First, develop a semi-analytical method based on the energy approach to predict the first few undamped natural frequencies and modes of annular-like disks. A bi-orthogonal shape function series is utilized in the Ritz minimization scheme and particular attention is paid to the prediction of elastic deformation shapes as they deviate from the flexural modes of classical annular plates. Finite element [26] and experimental modal analysis are used to validate the analytical prediction scheme. Second, study eigensolutions of many annular-like disks including a gear from the helicopter tail rotor gear box where at least 5% of the material has been removed (or added). Since designs with material removed are believed to be of more interest, circular holes or annular slots within the body (and not at the inner hubs or outer rims) are emphasized in our study. Only a few cases where the material is added at the outer and inner edges are considered which illustrate and verify the proposed approach. Third, examine the disk clamping boundary condition issue by using both experimental and analytical techniques.

An annular, elastic, stationary disk of outer radius r_o, inner radius r_i, and thickness h is the primary example are shown in Figure 1. The original annular disk is referred to as the blank that is described by space $\mathscr{R}_B$ of volume V_B. All of the N_H holes, slots, or cut outs are assumed to be within the body of the disk and not at the outer or inner rims. Combined together they are contained in a subspace $\mathscr{R}_H$ of control volume V_H. Similarly N_A elastic material attachments (within the body or at the inner or outer radius but without any mechanical joint or fastener) are characterized by subspace $\mathscr{R}_H$ of control volume V_A. Arbitrary boundary conditions σ_i and σ_o are assumed to exist at both r_i and r_o, respectively.

Geometric dimensions and other specifications of the example disk are given in Table 1 along with a list of various cases considered. Material removal or addition is quantified by Γ which is equal to $\Gamma = (V_A - V_H)/V_B$. Based on several practical designs, the range of $|\Gamma|$ is chosen to be from 0·05 to 0·6 which would preclude any crack-like incisions or very compliant ring-type disks. Table 1 lists typical Γ values considered in this study. It should however be noted that Γ is a global design quantifier since a specific Γ value may correspond to several annular-like disks with a wide variation in dynamic properties.

3. SEMI-ANALYTICAL RITZ METHOD

3.1. ENERGY FORMULATION

For the free vibration analysis, strain or potential (U) and kinetic (T) energies of the conservative, elastic disk of Figure 1 are expressed as follows:

$$U = U_B - U_H + U_A + U_\sigma - \left(\sum_{k=1}^{N_H} U_k\right)_{\mathscr{R}_H} + \left(\sum_{k=1}^{N_A} U_k\right)_{\mathscr{R}_A} + U_{\sigma_i\sigma_o},$$

$$T = T_B - T_H + T_A + T_\sigma - \left(\sum_{k=1}^{N_H} T_k\right)_{\mathscr{R}_H} + \left(\sum_{k=1}^{N_A} T_k\right)_{\mathscr{R}_A} + T_{\sigma_i\sigma_o}, \tag{1a, b}$$

where U_B and T_B are energy terms of the ideal annular blank with free–free boundary conditions; U_H and T_H represent energy contribution of the material which has been removed; U_A and T_A are energies due to the material added; and U_σ and T_σ are energy terms associated with realistic boundary conditions σ_i and σ_o at the inner (r_i) and outer (r_o) edges, respectively. Realistic boundaries may be viewed as deviations from the free edge(s) at r_i and r_0, i.e. datum, for U_σ and T_σ. The elastic deformation in flexure, at location (r, θ, z) on the disk, is described by the transverse displacement vector $\hat{\mathbf{f}}(r, \theta, z, t)$. Now, the potential and kinetic energies of the annular-like disk can be written as follows where $\mathbf{E}$ is the elastic Matrix, $\mathscr{D}$ is the differential operator matrix obtained from the compatibility and constitutive equations corresponding to a specific plate theory [17] and $\oint_V$ represents a volume integral:

$$U = \oint_{V_B} \tfrac{1}{2}(\mathscr{D}\hat{\mathbf{f}})^{\mathrm{T}}\mathbf{E}^{\mathrm{T}}(\mathscr{D}\hat{\mathbf{f}})\,\mathrm{d}V - \sum_{k=1}^{N_H} \oint_{V_H^k} \tfrac{1}{2}(\mathscr{D}\hat{\mathbf{f}})^{\mathrm{T}}\mathbf{E}^{\mathrm{T}}(\mathscr{D}\hat{\mathbf{f}})\,\mathrm{d}V + \sum_{k=1}^{N_A} \oint_{V_A^k} \tfrac{1}{2}(\mathscr{D}\hat{\mathbf{f}})^{\mathrm{T}}\mathbf{E}^{\mathrm{T}}(\mathscr{D}\hat{\mathbf{f}})\,\mathrm{d}V + (U)_{\sigma_i,\sigma_o},$$

$$T = \oint_{V_B} \tfrac{1}{2}\rho\dot{\hat{\mathbf{f}}}^{\mathrm{T}}\dot{\hat{\mathbf{f}}}\,\mathrm{d}V - \sum_{k=1}^{N_H} \oint_{V_H^k} \tfrac{1}{2}\rho\dot{\hat{\mathbf{f}}}^{\mathrm{T}}\dot{\hat{\mathbf{f}}}\,\mathrm{d}V + \sum_{k=1}^{N_A} \oint_{V_A^k} \tfrac{1}{2}\rho\dot{\hat{\mathbf{f}}}^{\mathrm{T}}\dot{\hat{\mathbf{f}}}\,\mathrm{d}V + (T)_{\sigma_i,\sigma_o}. \tag{2a, b}$$

It has been shown [1] that the classical thin plate theory is valid for thickness to width ratio $h/(r_o - r_i)$ below 0·1. For thicker plates, Mindlin and Dereshowitz [17, 18] have demonstrated that their theory, which includes rotary inertia and shear deformation effects, is applicable to a plate with thickness to width ratios between 0·1 and 0·7. Therefore the differential $\mathscr{D}$ and the elastic coefficient matrix $\mathbf{E}$ will be enumerated for both classical thin plate and Mindlin's thick plate theories. Each theory will be applied to annular-like disks and typical comparisons are given in later sections.

TABLE 1

Annular-disk cases studied given $r_o = 89{\cdot}4\ mm$, $r_i = 19{\cdot}98\ mm$ (except for cases 15), $E = 201\ GPa$, $\rho = 7800\ Kg/m^3$ and $\nu = 0{\cdot}28$. Boundary condition at r_o is free for all cases

Description	Example case	Pertinent dimensions mm or degrees	Disk thickness h (mm)	Γ	Boundary condition at r_i	
					Free	Clamped
Annular disk blank	1		6·35	0·0	x	
Disk with one hole (Fig. 5a)	2	$r_h = 55{\cdot}9$, $\xi = 19{\cdot}98$	6·35	−0·053		
Disk with one annular slot (Fig. 5b)	3	$\Delta r = 10$, $\Delta\theta = 129{\cdot}7^\circ$				
	4	$\Delta r = 20$, $\Delta\theta = 58{\cdot}9^\circ$				
	5	$\Delta r = 50$, $\Delta\theta = 17{\cdot}5^\circ$				
Disk with N_h holes (Fig. 5a) $N_h = 2$	6	$r_n = 55{\cdot}9$, $\xi = 24{\cdot}7$	6·35	−0·158	x	
$N_h = 3$	7	$\xi = 20{\cdot}0$				
$N_h = 4$	8	$\xi = 17.3$				
$N_h = 9$	9	$\xi = 12{\cdot}3$				
Annular disk blank	10		6·35	0·0		x
Annular disk blank	11		3·175	0·0	x	x
Disk with material added at the outer rim (Fig. 12a)	12	$r_R = 76{\cdot}2$ $h_R = 6{\cdot}35$	3·175	0·576	x	
Disk with material added at inner and outer rims (Fig. 12b)	13	$r_R = 76{\cdot}2$, $h_R = 6{\cdot}35$ $r_Q = 32{\cdot}5$, $h_Q = 6{\cdot}35$	3·175	0·603	x	
Disk with both material added (outer thick rim) and material removed (two holes) (Fig. 15)	14	$N_h = 2$, $r_h = 48{\cdot}0$ $\xi = 24{\cdot}64$ $r_R = 76{\cdot}2$, $h_R = 6{\cdot}35$	3·175	0·322	x	
Helicopter transmission gear. Thick outer rim with gear teeth and thick inner hub with splines (Figs 16 and 17)	15	$N_h = 8$, $r_h = 6{\cdot}5$ $r_R = 42{\cdot}0$, $h_R = 4{\cdot}6$ $r_Q = 22{\cdot}0$, $h_Q = 17{\cdot}4$	3·220	0·26	x	
r_o is both pitch diam.		$r_o = 52$				
$r_i$is pitch diam. [spline]		$r_i = 19$				

From the classical thin plate theory [1] the matrices $\mathscr{D}$ and $\mathbf{E}$ are as follows in the cylindrical coordinate (r, θ, z) system where E is the Young's modulus and v is Poisson's ratio:

$$\mathscr{D} = \begin{bmatrix} -z\dfrac{\partial^2}{\partial r^2} \\ -\dfrac{z}{r^2}\dfrac{\partial^2}{\partial \theta^2} - \dfrac{z}{r}\dfrac{\partial}{\partial r} \\ -2\dfrac{z}{r}\dfrac{\partial^2}{\partial r\,\partial \theta} + 2\dfrac{z}{r^2}\dfrac{\partial}{\partial \theta} \end{bmatrix}, \qquad \mathbf{E} = \begin{bmatrix} \dfrac{E}{1-v^2} & \dfrac{Ev}{1-v^2} & 0 \\ \dfrac{Ev}{1-v^2} & \dfrac{E}{1-v^2} & 0 \\ 0 & 0 & \dfrac{E}{2(1+v)} \end{bmatrix}. \quad (3a, b)$$

The differential operator and elastic matrices for the Mindlin's thick plate theory [17] are as follows (here a shear correction factor of $\pi^2/12$ has been used):

$$\mathscr{D} = \begin{bmatrix} \partial/\partial r & 0 & 0 \\ 1/r & (1/r)\partial/\partial\theta & 0 \\ (1/r)\partial/\partial\theta & \partial/\partial r - 1/r & 0 \\ \partial/\partial z & 0 & \partial/\partial r \\ 0 & \partial/\partial z & (1/r)\partial/\partial\theta \end{bmatrix},$$

$$\mathbf{E} = \begin{bmatrix} E/(1-v^2) & Ev/(1-v^2) & 0 & 0 & 0 \\ Ev/(1-v^2) & E/(1-v^2) & 0 & 0 & 0 \\ 0 & 0 & E/(2(1+v)) & 0 & 0 \\ 0 & 0 & 0 & E\pi^2/(24(1+v)) & 0 \\ 0 & 0 & 0 & 0 & E\pi^2/24(1+v)) \end{bmatrix}. \quad (4a, b)$$

3.2. MASS AND STIFFNESS MATRICES

The deformation vector $\hat{\mathbf{r}}$ can be approximated as

$$\hat{\mathbf{r}}(r, \theta, z, t) \cong \mathbf{S}(r, \theta, z)\mathbf{q}_f(t), \quad (5)$$

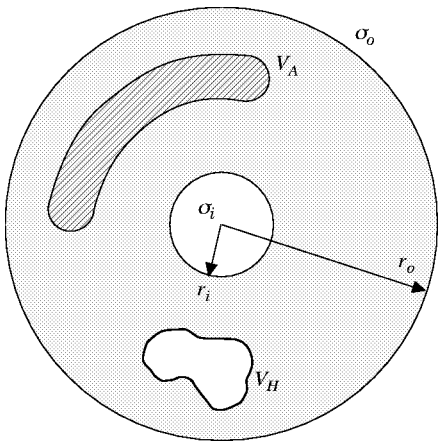

Figure 1. Example case: annular-like disk with material removed (of volume V_H) and added of volume V_A), and arbitrary boundary conditions (σ_i and σ_o).

where $\mathbf{S}$ is the shape function matrix and $\mathbf{q}_f(t)$ is the generalized flexible coordinate vector of the disk. Using equations (3) and (4), the strain and kinetic energies can be written as

$$U \cong \tfrac{1}{2}\mathbf{q}_f^{\mathrm{T}}[\mathbf{K}_B - \mathbf{K}_H + \mathbf{K}_A]\mathbf{q}_f + \mathbf{U}_\sigma, \qquad T \cong \tfrac{1}{2}\dot{\mathbf{q}}_f^{\mathrm{T}}[\mathbf{M}_B - \mathbf{M}_H + \mathbf{M}_A]\dot{\mathbf{q}}_f + \mathbf{T}_\sigma, \tag{6a, b}$$

where the various stiffness ($\mathbf{K}$) and mass ($\mathbf{M}$) matrices are defined as

$$\mathbf{K}_B = \oint_{V_B} \mathbf{S}^{\mathrm{T}}(r, \theta, z)\mathbf{E}^{\mathrm{T}}\mathbf{S}(r, \theta, z)\,\mathrm{d}V; \qquad \mathbf{K}_H = \sum_{k=1}^{N_H} \mathbf{K}_{H_k},$$

$$\mathbf{K}_{H_k} = \oint_{V_{H_k}} \mathbf{S}^{\mathrm{T}}(r, \theta, z)\mathbf{E}^{\mathrm{T}}\mathbf{S}(r, \theta, z)\,\mathrm{d}V. \tag{7a, b}$$

$$\mathbf{K}_A = \sum_{k=1}^{N_A} \mathbf{K}_{A_k}, \qquad \mathbf{K}_{A_k} = \oint_{V_{H_k}} \mathbf{S}^{\mathrm{T}}(r, \theta, z)\mathbf{E}^{\mathrm{T}}\mathbf{S}(r, \theta, z)\,\mathrm{d}V;$$

$$\mathbf{M}_B = \oint_{V_B} \rho\mathbf{S}^{\mathrm{T}}(r, \theta, z)\mathbf{S}(r, \theta, z)\,\mathrm{d}V. \tag{7c, d}$$

$$\mathbf{M}_H = \sum_{k=1}^{N_H} \mathbf{M}_{H_k}, \qquad \mathbf{M}_{H_k} = \oint_{V_{H_k}} \rho\mathbf{S}^{\mathrm{T}}(r, \theta, z)\mathbf{S}(r, \theta, z)\,\mathrm{d}V,$$

$$\mathbf{M}_A = \sum_{k=1}^{N_A} \mathbf{M}_{A_k}, \qquad \mathbf{M}_{A_k} = \oint_{V_{A_k}} \rho\mathbf{S}^{\mathrm{T}}(r, \theta, z)\mathbf{S}(r, \theta, z)\,\mathrm{d}V. \tag{7e, f}$$

Further, the boundary conditions are defined by the contact stiffness and mass loading per unit are in terms of $k_\sigma(r, \theta, z)$ and $m_\sigma(r, \theta, z)$, respectively, distributed over a boundary regime of area A_σ; a detailed discussion of this topic can be found in Section 5.3. Energy terms and corresponding matrices are

$$U_\sigma = \tfrac{1}{2}\mathbf{q}_f^{\mathrm{T}}(t)\mathbf{K}_\sigma\mathbf{q}_f(t), \qquad \mathbf{K}_\sigma = \int_{A_\sigma} \mathbf{S}^{\mathrm{T}}(r, \theta, z)k_\sigma(r, \theta, z)\mathbf{S}(r, \theta, z)\,\mathrm{d}A,$$

$$T_\sigma = \tfrac{1}{2}\dot{\mathbf{q}}_f^{\mathrm{T}}(t)\mathbf{M}_\sigma\dot{\mathbf{q}}_f(t), \qquad \mathbf{M}_\sigma = \int_{A_\sigma} \mathbf{S}^{\mathrm{T}}(r, \theta, z)m_\sigma(r, \theta, z)\mathbf{S}(r, \theta, z)\,\mathrm{d}A. \tag{8a–d}$$

One can assemble all of the above mentioned parameter matrices, and define the effective stiffness ($\mathbf{K}$) and mass ($\mathbf{M}$) matrices of the annular-like disk as

$$\mathbf{K} = \mathbf{K}_B - \mathbf{K}_H + \mathbf{K}_A + \mathbf{K}_\sigma, \qquad \mathbf{M} = \mathbf{M}_B - \mathbf{M}_H + \mathbf{M}_A + \mathbf{M}_\sigma. \tag{9a, b}$$

The eigenvalue problem, $|\omega^2\mathbf{I} + \mathbf{M}^{-1}\mathbf{K}| = 0$, yields undamped natural frequencies ω_r and elastic modes of deformation ψ_r where r is the modal index and $\mathbf{I}$ is the identity matrix. The natural frequency, $\omega_r(\mathrm{rad/s}) = 2\pi f_r$ (Hz) results will be given in terms of the dimensionless eigenvalue parameter $\lambda_r^2 = \omega_r r_0^2\sqrt{\rho h/D}$ and $D = Eh^3/12(1 - \nu^2)$; refer to Leissa [1]. Mode shapes will be normalized (ψ_r) by amplitude scaling.

3.3. ADMISSIBLE FUNCTIONS

Energy principle and Rayleigh-Ritz minimization schemes, in various forms, have been commonly employed to study circular, annular and arbitrarily shaped plates

[1, 4–11, 21–24]. Also, several classes of admissible shape functions have been utilized depending upon the geometry and boundary conditions of the plates being analyzed. For instance Liew *et al*. [7, 8, 24] have developed a pb-2 function where p-2 indicates a two-dimensional polynomial and b is a base function satisfying the essential boundary conditions such that pb-2 is unconditionally admissible. Kitipornchai *et al*. [6] have used this function in conjunction with a modified Ritz method to analyze Mindlin plates of arbirtrary shape with non-classical boundary conditions. Liew and Xiang [7] have analyzed annular Mindlin plates with ring supports using pb-2 functions, and Liew [15] solved for the natural frequencies and mode shapes of a trapezoidal plate of variable thickness using these functions. Another bi-orthogonal shape function has been proposed by Singh *et al*. [9] through the Gram-Schmidt iterative process. Mote *et al*. [4, 5] have utilized the perturbation analysis for circular plates with slight irregularities. In particular, Yu and Mote [4], and Shen and Mote [5] investigated the effect of edge slots and small inhomogeneous elastic inclusions in the body of the structure on the dynamic response of plates. Perturbed forms of classical dynamic governing equations are described which estimate natural frequencies and mode shapes. Yet, another solution methodology that has been recently reported by Wang *et al*. [10] and Larrondo [11] is the differential quadrature (DQ) process. This is essentially a numerical strategy through which the weighting coefficients and their derivatives are obtained for high order polynomials. Polynomial shape functions have been used to avoid the Bessel functions which cause numerical problems in further analytical studies such as the calculation of sound radiation from annular plates [20]. Finally, Oosterhout *et al*. [23] have discussed computational issues related to the determination of higher modes.

Vibration mode shapes ψ_{mn} of an annular disk with classical boundary conditions (free, fixed or simply supported) are given as follows where m is the number of nodal circles and n is the number of nodal diameters [1, 4, 5]:

$$\psi_{mn}(r, \theta) = P_{mn}(r)\begin{Bmatrix}\cos(n\theta + \theta_{o_{mn}})\\ \sin(n\theta + \theta_{o_{mn}})\end{Bmatrix}, \tag{10}$$

where P_{mn} is given by a linear combination of Bessel functions and θ_o is arbitrary only for repeated modes. Yu and Mote [4] give an expression for θ_o for radial slots at the outer rim. The same (m, n) terminology is retained for the annular-like disk but recognize that gross changes within the structure of a disk will significantly change the elastic modes such that it may not be possible to describe the resulting eigenvector by perturbation analysis and other existing analytical modal bases. A new bi-orthogonal admissible basis that consists of polynomial and trigonometric shape functions is proposed as follows:

$$\mathbf{S}(r, \theta, z) = [S_1(r, \theta, z) \quad S_2(r, \theta, z) \quad \cdots \quad S_i(r, \theta, z) \quad \cdots \quad S_{N_S}(r, \theta, z)],$$

$$S_i(r, \theta, z) = P_k(r)\Theta_l(\theta), \qquad k = 0, \ldots, N_r; \quad l = 0, \ldots, N_\theta;$$

$$N_S = (N_r + 1)(N_\theta + 1); \quad i = lN_r + k + 1 = 1, \ldots, N_S, \tag{11a–f}$$

where $P_k(r)$ and $\Theta_l(\theta)$ are defined as

$$P_k(r) = \left\{\sum_{j=0}^{k} b_j \frac{(r - r_i)^j}{(r_0 - r_i)^j} \in \mathscr{P}^k(r): \langle P_p, P_q\rangle_r = \int_{r_i}^{r_o} P_p P_q r \, \mathrm{d}r = \delta_{pq}\right\}, \tag{12a}$$

$$p = 0, 1, \ldots, N_r; \qquad q = 0, 1, \ldots, N_r;$$

and

$$\Theta_l(\theta) = \left\{ \begin{cases} \cos(l/2)\theta & \text{if } l \text{ is even} \\ \sin[(l+1)/2]\theta & \text{if } l \text{ is odd} \end{cases} : \langle \Theta_f, \Theta_g \rangle_\theta = \int_0^{2\pi} \Theta_f \Theta_g \, \mathrm{d}\theta = \delta_{fg} \right\} \tag{12b}$$

$$f = 0, 1, \ldots, N_\theta; \qquad g = 0, 1, \ldots, N_\theta;$$

Here, $\mathscr{P}^k(r)$ is a polynomial of order k and

$$\delta_{pq} = \begin{cases} 1 & \text{if } p = q \\ 0 & \text{if } p \neq q \end{cases}.$$

An inner product is defined over the (r, θ) domain by noting that $\mathrm{d}\bar{r} \perp r \, \mathrm{d}\bar{\theta}$:

$$\langle S_i, S_j \rangle_{r,\theta} = \langle P_p \Theta_f, P_q \Theta_g \rangle_{r,\theta} = \langle P_p, P_q \rangle_r \langle \Theta_f, \Theta_g \rangle_\theta, \qquad i = fN_r + p + 1,$$
$$j = gN_r + q + 1. \tag{13}$$

Therefore $\{S_i\}_0^{N_s}$ is a bi-orthogonal set with respect to $\langle S_i, S_j \rangle_{r,\theta} = \int_{r_i}^{r_0} \int_0^\pi S_i S_j r \, \mathrm{d}\theta \, \mathrm{d}r$. Hence,

$$\langle S_i, S_j \rangle_{r,\theta} = \langle P_p \Theta_f, P_q \Theta_g \rangle_{r,\theta} \neq 0, \quad \text{if } p = q \vee f = g. \tag{14}$$

It is conceivable that the mode shapes of annular-like disks may not be described by equation (10). However for the sake of comparison, the calculated mode shapes $\Psi_r(r, \theta)$ will be compared to the corresponding classical (m, n) modes of an annular disk, with free–free or fixed–free boundaries. But the nth circumferential mode for annular-like disks is now given by a combination of trigonometric functions, i.e. $\sin(n\theta)$, $\sin(2n\theta)$, $\sin(3n\theta)$, . . . , as opposed to only one $\sin(n\theta)$ term in equation (10) for a regular annular plate. The mode shape $\Theta_l(\theta)$ is still periodic but it contains many terms which are dictated by the nature and amount of material removed or added. Similarly, the polynomial series for $P_k(r)$ may be of a high order. The total number of terms (N_r and N_θ) which must be included in equation (11) for a reasonably accurate analysis is somewhat problem specific and related to disk geometry, boundary conditions and frequency range of interest. It will be illustrated later via examples.

A two-dimensional Gauss point integration technique was used for calculations. It was found to be both fast and accurate for this problem. Nevertheless care must be taken in choosing the order of Gauss points, such that enough resolution is maintained to accurately represent the irregular geometry including discontinuities while keeping the calculation time to be reasonable. In addition to geometric considerations, the nature and order of shape functions being integrated also become critical. For example, a Gauss point integration order of 30 was required to successfully obtain the (1, 0) more for a disk with one hole but an order of 10 was sufficient to achieve the same accuracy for the mode for a regular disk with no geometric irregularities.

4. STUDY OF FREE–FREE ANNULAR DISK BLANKS

Many steel blanks, given the same nominal dimensions which are listed in Table 1, were fabricated and experimentally evaluated as a part of this study (for cases 1–14) before cutting any holes or slots. Two specific boundary conditions at r_i are chosen while the outer edge at r_o is always kept free. Natural frequencies ω_r and modes ψ_r are obtained by using closed form solutions [1], a semi-analytical approach (designated as Ritz), the finite element method (FEM), and experimental modal testing (Expt.) The FEM models of cases 1–11 were constructed by using 8-noded elements and about 100 master-degrees-of-freedom were specified to extract 20 modes [26]. The computational time of the Ritz method was

TABLE 2

Natural frequencies of a free–free annular disk (case 1)

Modes		Natural frequencies λ^2				
m, n	r	Experimental	Ritz (Cl. thin)	Ritz (Mindlin's plate theory)	FEM	Classical thin [1]
0, 2	1	5·07	5·04	5·00	5·04	5·04
	2	5·07	5·04	5·00	5·01	5·04
1, 0	3	8·24	8·21	8·16	8·25	8·20
0, 3	4	12·21	12·23	12·03	12·21	12·20
	5	12·21	12·23	12·03	12·26	12·20
1, 1	6	18·64	18·99	18·39	18·68	19·00
	7	18·64	18·99	18·39	18·80	19·00

m = number of nodal circles, n = number of nodal diameters.

observed to be at least one order of magnitude than that of FEM, for all example cases considered.

Table 2 compares the eigenvalue parameter λ^2 results obtained from various analyses with those measured for a free–free annular disk (case 1) whose dimensions are given in Table 1. Experimental results based on 7 blank samples show a minor variation in eigenvalues for various modes. The λ^2 values are rounded-off to be within $\pm 0{\cdot}01$, which is about ± 2 Hz for the example cases considered in this paper. All analyses predict natural frequencies and modes reasonably well. Observe that the Ritz method employing either the thick (Mindlin) or thin (classical) plate theory yields virtually the same results even though the thickness to width ratio $= h/(r_o - r_i) = 0{\cdot}09$ is at the threshold of the applicability range of thin plate theory [1]. Mindlin's plate theory has been applied to several other cases of Table 1 but in each instance both theories predicted virtually the same results. As a consequence, further results are based on the classical thin plate theory.

5. CLAMPED BOUNDARY ISSUES

5.1. LITERATURE REVIEW

In rotating equipment, annular disks are often mounted on shafts, rotors or spindles by collars, splines or through interference fits depending on the application. D'Angelo and Mote have surveyed the literature for models that describe the clamped boundary condition at the inner edge r_i of thin plates and disks [12]. Three common models, namely the zero displacement (ideally fixed), zero stress and finite stress, were quantitatively compared for a disk of $r_0 = 712$ mm, $r_i = 127$ mm and $h = 0{\cdot}775$ mm. All models exhibited errors in their prediction capabilities, some of the order of 10% depending on the vibration mode. To improve the natural frequency predictions of a disk rotating at high speeds they suggested inclusion of contact friction effects.

Hayashi *et al*. have examined thick annular plates which are solidly mounted on shafts without any clamps or splines; disk and shaft were fabricated as an integral unit [13, 14]. The zero displacement or ideally fixed boundary condition model yielded errors of 10 to 25% for a plate of $r_o = 200$ mm, $r_i = 50$ or 75 mm and $h = 5$, 15 or 25 mm. Instead they developed a model that assumed the disk to be elastically supported at r_i. Equivalent spring constants were obtained through an approximate analysis of a semi-infinite body under the influence of a moment load. Their predictions, based on the Mindlin's thick plate theory, improved significantly with the new clamp interface model. For instance, about

1% error was observed for the (0, 3) mode, even up to 22% error was seen for other modes such as the (1, 1) mode. One of their examples also included a helical gear of thickness to diameter ratio 0·2 that was mounted on a shaft; no holes or material additions were considered within the gear body. Their model was reasonably effective as discrepancies of 2 to 18% were found between measured and calculated natural frequencies.

5.2. CLAMPING EXPERIMENTS

To simulate the inner edge (r_i) mounting, a clamped experiment was designed as a part of this investigation; the outer edge (r_o) was kept free. The first clamp of Figure 2(a) was the original design, but measurements showed that due to impecise axial positioning of the bolt, it was virtually impossible to apply a consistent clamping force. As a consequence, a large variations in natural frequency of the clamped disk between successive assembly and disassembly was observed. The clamp was then redesigned and designated as the second clamp in Figure 2(b). An axially positioned ring was introduced between the bolt and the plate that resulted in a consistent clamping force. Measured eigenvalues for both clamps are listed in Table 3(a) in terms of mean and standard deviations obtained for a sample size of 10 disk-lamp assemblies. Note that the mean values of λ_r^2 for all of the

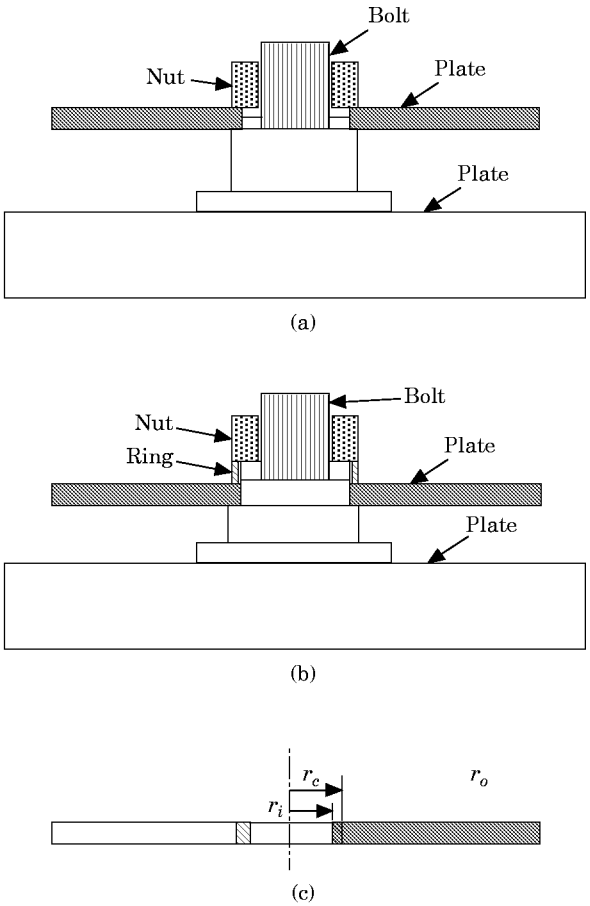

Figure 2. Schematic of the experiments designed to simulate the clamped boundary condition at the inner edge. (a) First clamp design, (b) second clamp design, (c) illustration of the clamping contact zone.

TABLE 3

Natural frequencies of clamped–free annular disk (*Case* 10). (*A sample size of* 10 *disk assemblies was used for measurements*)

(a) *Comparison between first and second clamp designs of Figure* 2. *Predictions based on Model I of Figure* 3 *are also compared with material data*.

Mode		Experimental λ^2				Calculated λ^2 based on ideal boundary conditions (Model I of Figure 3)	
		First clamp		Second clamp			
m, n	r	Mean	St. Dev.	Mean	St. Dev.	at $r = r_i$	at $r = r_c$
0, 1	1	4·1	0·144	3·9	0·082	5·2	5·7
	2	4·2	0·089	4·0	0·078	5·2	5·7
0, 0	3	4·8	0·076	4·7	0·051	5·4	5·9
0, 2	4	6·3	0·051	6·1	0·030	6·8	7·3
	5	6·3	0·066	6·1	0·029	—	—
1, 0	6	12·6	0·031	11·4	0·013	12·8	13·0
0, 3	7	N/A	N/A	12·5	0·013	12·8	13·0
	8	N/A	N/A	12·5	0·015	12·8	13·0

(b) *Comparison between clamp models of Figure* 3. *All predictions employ the Ritz method based on thin plate theory*. *Experimental results are for the second clamp only*.

Mode		λ^2 (Expt.)	λ^2 (Ritz)					
m, n	r	Mean	Model II	ϵ%	Model III	ϵ%	Model IV	ϵ%
0, 1	1	3·9	4·0	1·2	4·4	11·8	4·0	1·6
	2	4·0	4·0	0·0	4·4	10·5	4·0	0·4
0, 0	3	4·7	4·3	−7·8	5·1	9·6	4·7	−0·6
0, 2	4	6·1	6·4	4·6	6·4	4·3	5·8	−4·9
	5	6·1	6·4	4·5	6·4	4·2	5·8	−5·0
1, 0	6	11·4	9·7	−14·6	12·3	7·7	10·5	−7·9
0, 3	7	12·5	13·0	3·7	12·9	2·8	11·8	−6·0
	8	12·5	13·0	3·7	12·9	2·8	11·8	−6·0

N/A = Not measured; $\epsilon\% = 100 \times (\lambda^2(\text{Experimental}) - \lambda^2(\text{Ritz}))/\lambda^2(\text{Experimental})$.

modes are much higher for the first clamp but so are the standard deviations. For instance, mean and standard deviation of the lowest natural frequency for the first clamp were 796 Hz and 28 Hz. In contrast, the second clamp yielded a mean and standard deviation of 757 Hz and 16 Hz. Standard deviations for higher modes were relatively smaller for both clamps. Therefore the second clamp was chosen for subsequent work. When all of the experimental and calculation uncertainties are considered, it is appropriate to truncate the eigenvalues to within $\pm 0{\cdot}1$; this would correspond to approximately 20 Hz for the cases of Table 1.

5.3. CLAMPING MODELS

Identification of appropriate boundary conditions is obviously necessary before any realistic mathematical model can be constructed, as also suggested by Pabst and Hagedorn [25] in an article that appeared after the completion of work reported here. Clamped–free annular disk is examined first by using the ideal boundary condition model at the inner edge. As depicted in Figures 2 and 3, radial displacement may be assumed to be zero at $r = r_i$ or $r = r_c$ because of the finite contact annulus. It is designated as Model I in Figure 3

and Table 3(a). A significant discrepancy is noted between measured and computed natural frequencies. For example, measured frequencies for the (0, 1) mode are 757 and 776 Hz for two clamps, and the corresponding predictions are 1003 Hz for Model I with $r_i = 19{\cdot}98$ mm and 1107 Hz with $r_c = 23$ mm. Higher modes including (0, 0), (0, 2) and (0, 3) show somewhat lower but still significant errors in predictions. For instance, 1190 Hz was measured for the (0, 2) mode with the second clamp, and Model I predicted 1320 Hz with clamping at $r = r_i$. In fact, some of the modeling errors are higher than observed previously by D'Angelo and Mote [12] and Hayashi [13, 14] in their investigations. Given the inadequacy of zero displacement idealization (Model I), other models as available in the literature were carefully reviewed. The elastic boundary condition theory proposed by Hayashi *et al*. [13] seemed most plausible for our experiment and hence it was first implemented. Model II describes this case but unlike lumped springs of Hayashi *et al*. [13] a distributed stiffness model is proposed over the contact regime from r_i to r_c. A uniform stiffness loading k_σ is assumed as designated in Model II of Figure 3(c). It is obtained numerically by equating the total stiffness $\int_0^{2\pi}\int_{r_i}^{r_o} k_\sigma(r, \theta)\,\mathrm{d}r\,\mathrm{d}\theta = 2\pi\bar{k}_\sigma(r_c - r_i)$ to the combined longitudinal stiffness of bolt, ring and the clamp post. A numerical value of

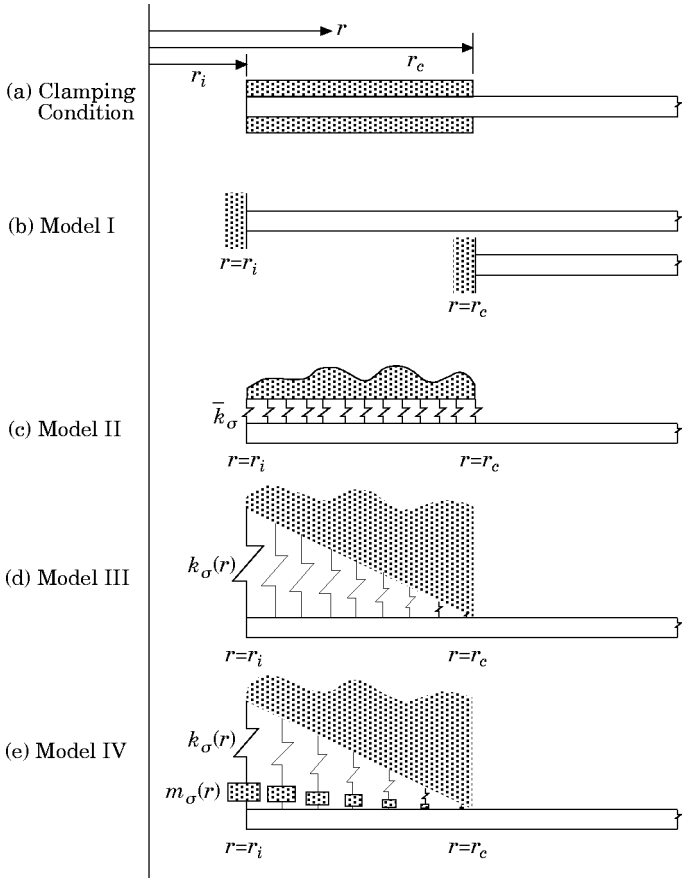

Figure 3. Models used to describe the clamping contact regime of Figure 2(c). (a) Clamping condition, (b) ideal boundary condition at r_i or r_o (Model I), (c) uniform stiffness loading (Model II), (d) non-uniform stiffness loading (Model III), (e) non-uniform stiffness and mass loading (Model IV).

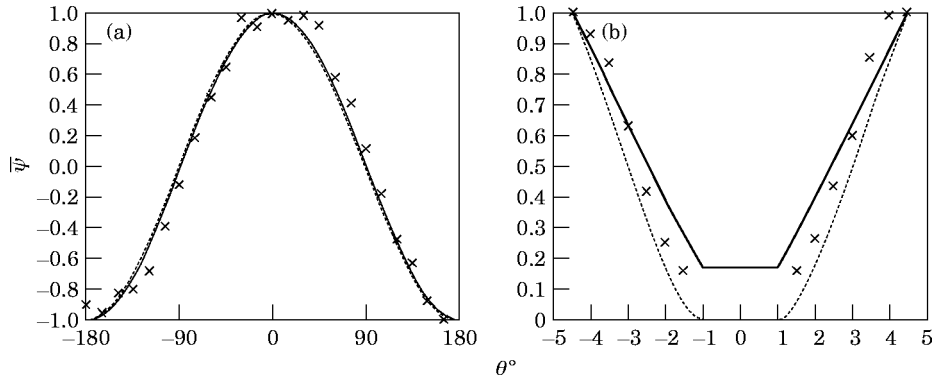

Figure 4. Comparison of mode shapes for the annular disk with clamped inner edge (case 10). Here $\bar{\psi}$ is the normalized mode shape, θ° is the angular position in degrees and $\bar{r} = r/r_i$. (a) Mode (0, 1) at $r = r_o$, (b) mode (0, 0) at $\theta = 0^\circ$. Key: ×, experimental; . . . . , Ritz (Model I); ——, Ritz (Model IV).

$\bar{k}_c = 0{\cdot}34$ GPa/m was found for the second clamping experiment. From equations (8a, b), the strain energy is now given as follows where A_σ is the clamp contact area while T_{σ_i} is still zero:

$$U_{\sigma_i} = \tfrac{1}{2}\,\mathbf{q}_f^{\mathrm{T}}(t)\left[\int_{A_\sigma} \mathbf{S}^{\mathrm{T}}(r,\theta,z)k_\sigma(r,\theta,z)\mathbf{S}(r,\theta,z)\,\mathrm{d}A_\sigma\right]\mathbf{q}_f(t). \tag{15}$$

The eigenvalues λ^2 obtained from Model II are listed in Table 3(b). Though this model predicts the first mode well, predictions for higher modes deviate appreciably from experimental results. Therefore another clamp model with radially varying clamping stiffness was developed (Model III of Figure 3(d)) with the contact stiffness loading given by the following

$$k_\sigma(r,\theta,z) = \bar{k}(r_i)\,\frac{(r_C - r)}{(r_C - r_i)}. \tag{16}$$

In Model III, $\bar{k}_c = 0{\cdot}34$ GPa/m was used to predict the λ^2, which are also listed in Table 3(b). The discrepancy between theory and experiment is still large but it predicts certain modes better and others worse than Model II even though both are superior to Model I. Further improvements in the prediction capability are achieved by recognizing that an impedance boundary condition exists in the experiment as opposed to only elastic supports at the clamped edge. Consequently, Model IV of Figure 3(e) is proposed which also includes kinetic energy T_{σ_i} associated with the clamping contact regime dynamics; but damping is excluded. It is described as

$$T_{\sigma_i} = \tfrac{1}{2}\dot{\mathbf{q}}_f^{\mathrm{T}}(t)\left[\int_{A_\sigma} \rho\mathbf{S}^{\mathrm{T}}(r,\theta,z)m_\sigma(r,\theta,z)\mathbf{S}(r,\theta,z)\,\mathrm{d}A_\sigma\right]\dot{\mathbf{q}}_f(t), \quad m_\sigma(r,\theta,z) = \bar{m}_\sigma(r_i)\,\frac{(r_C - r)}{(r_C - r_i)}. \tag{17a, b}$$

Natural frequencies as predicted by Model IV compare very well with measured data as evident from Table 3(b). In fact, the error for the first 3 eigenvalues corresponding to the (0, 1) and (0, 0) modes is very small, while only a discrepancy of 5 to 8% is seen over the remaining modes of interest. Excellent comparisons are also found between Model IV and experimental mode shapes, as seen from the sample plots presented in Figure 4. Mode shapes corresponding to Model I (ideal boundary condition) are also plotted as

benchmark. Further detailed studies of annular-like disks were conducted with free–free boundary conditions for the sake of convenience. However, two additional cases (11 and 14) were experimentally examined with clamped inner edges; these will be discussed in Section 7.2.

6. DISKS WITH CIRCULAR HOLES OR ANNULAR SLOTS

To study the effects of material removal on the eigensolutions of an annular disk, circular holes or annular slots were cut into the blank as shown in Figure 5. All cases (2–9) of Table 1 with free–free boundary conditions are analyzed by using the proposed Ritz method, and results are compared with those from experimental modal analysis (Expt) and finite element method (FEM).

6.1. EFFECT OF ONE CIRCULAR HOLE (CASE 2)

Table 4 presents eigenvalues for this case as predicted by the semi-analytical Ritz method for both classical thin and Mindlin's thick plate theories. Both calculations show good agreements with measured natural frequencies. In fact, the Ritz method is as good, if not better, in predicting all modes while being more computationally efficient than FEM. For the sake of comparison, annular plate (case 1) results are also listed in this table. Observe that one circular hole lowers the natural frequencies and splits several repeated eigenvalues. Strictly speaking the modal indices (m, n) are no longer valid since the normalized modal shapes $\overline{\psi}_r(r, \theta, z)$ of an annular-like disk may significantly deviate from those of an annular plate as illustrated by Figures 6 and 7. Also a strong coupling between modal displacements in the radial (r) and circumferential (θ) directions may be seen. Nonetheless the (m, n) indices are used throughout in order to maintain consistency between various cases and to demonstrate how each mode may be affected.

Figure 6 compares the normalized displacement shapes $\overline{\psi}$ for the $(0, 2)$ mode, as obtained by Ritz method, experiment and FEM. Excellent correlation between all results is seen. Minor changes in the mode shape as introduced by one hole are observed when the results are compared with the annular plate (case 1) mode. However, more dramatic changes can be seen in Figure 7 corresponding to the $(1, 0)$ mode. The Ritz method accurately predicts angular variations in modal displacements at the outer (r_o) and inner (r_i) edges as depicted in Figures 7(a) and (b), respectively. It is clear that the changes

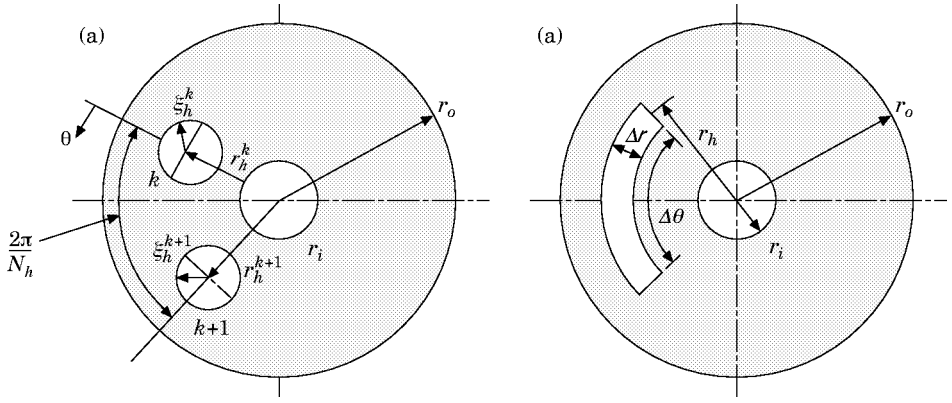

Figure 5. Annular disk with material removed. (a) N_H circular, equally spaced identical holes (cases 2, 6–9), (b) one annular slot.

TABLE 4

Natural frequencies of a free–free annular disk with holes and annular slots. Refer to Table 1 *and Figure* 5

Mode		Natural frequencies λ^2													
		Annular Blank Case 1 ($\Gamma = 0{\cdot}000$)			One Hole Case 2 ($\Gamma = -0{\cdot}053$)				One Annular slot Case 3 ($\Gamma = -0{\cdot}053$)			Three Holes Case 7 ($\Gamma = -0{\cdot}158$)			
m, n^*	r	Expt.	Ritz	FEM	Expt.	Ritz[1]	Ritz[2]	FEM	Expt.	Ritz	FEM	Expt.	Ritz[1]	Ritz[2]	FEM
0, 2	1	5·1	5·1	5·1	4·9	4·9	4·9	5·0	5·0	5·0	4·9	4·6	4·7	4·7	4·6
	2	5·1	5·1	5·1	4·9	4·9	4·9	5·0	5·0	5·0	4·9	4·7	4·7	4·8	4·6
1, 0	3	8·3	8·3	8·4	7·9	7·9	8·0	8·2	7·7	8·1	7·7	6·9	7·2	7·4	7·0
0, 3	4	12·4	12·4	12·3	11·8	11·9	11·9	12·1	11·7	12·1	11·7	11·0	11·2	11·4	11·0
	5	12·4	12·4	12·3	11·9	12·1	12·1	12·2	11·9	12·1	11·9	11·5	11·7	11·9	11·6
1, 1	6	18·8	19·3	19·0	18·0	18·5	17·7	18·6	16·6	17·8	16·7	16·7	17·6	17·1	16·8
	7	18·8	19·3	19·1	18·0	18·6	18·1	19·1	18·0	19·0	16·7	16·7	17·6	17·1	16·9
0, 4	8	21·5	21·9	21·6	20·7	21·1	21·0	21·4	21·0	21·4	20·9	19·8	20·5	20·5	19·9
	9	21·5	21·9	21·6	5·4	21·1	21·1	21·6	21·0	21·4	21·0	19·8	20·5	20·5	20·0

* Simplified mode shapes corresponding to annular plate (case 1); m = number of nodal circles; n = number of nodal diameter.
[1] Classical thin plate theory; [2]Mindlin's thick plate theory.

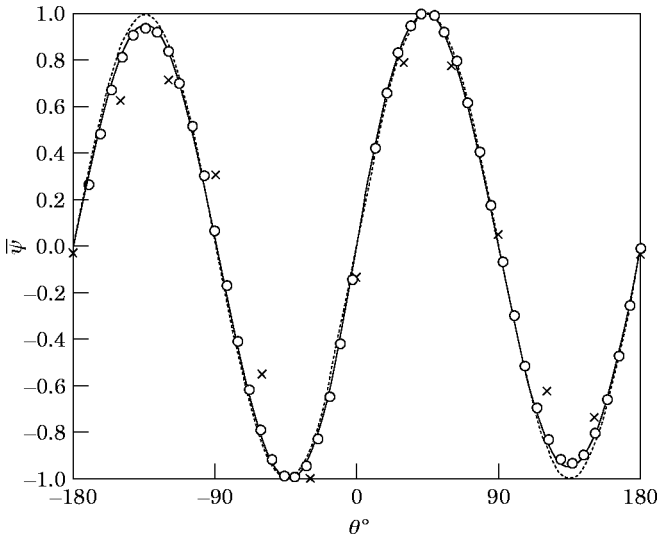

Figure 6. Comparison of mode shapes for the annular disk with one hole (case 2, free–free). Mode (0, 2) at $r = r_o$. Key: ×, experimental; ○, FEM; ——, Ritz; · · · ·, case 1.

observed in $\bar{\Psi}_r(r, \theta)$ are major and hence perturbation or assumed mode shape type analyses [1, 5] are not suitable for such annular-like disks.

6.2. EFFECT OF NUMBER OF SHAPE FUNCTIONS

Recalling from equations (11–14) that the shape function matrix $\mathbf{S}(r, \theta, z)$ is defined by a bi-orthogonal set of N_s distinct terms where $N_s = (N_r + 1)(N_\theta + 1)$. It is difficult to know *a priori* how many N_r and N_θ terms are necessary for an annular-like disk because this determination is, as mentioned before, problem specific. For instance, many terms are needed for a case with several geometric discontinuities, and a very few terms are sufficient for a disk that is virtually identical to an annular plate. An excessive number of terms in the expansion would obviously negate the goal of a computationally efficient Ritz method. Some guidelines are, however, presented here to aid future analyses. For the sake of illustration, again consider the Ritz method for case 2 with various N_r and N_θ terms. Figure 8 compares results for the (0, 1) mode shown previously in Figure 7(a). Observe

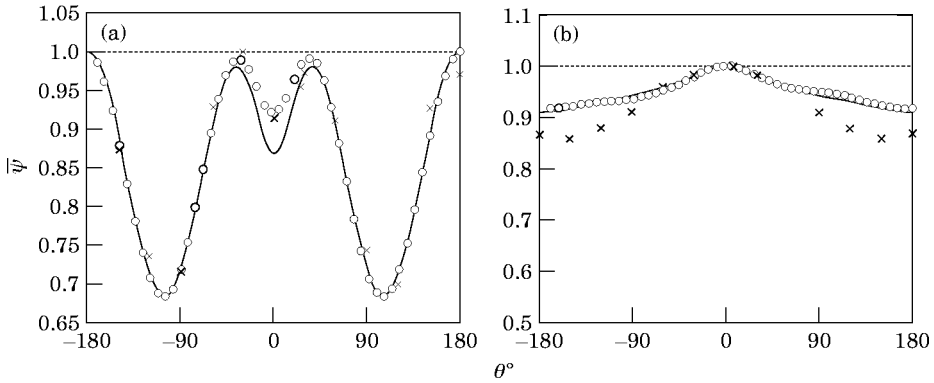

Figure 7. Comparison of mode shapes for the annular disk with one hole (case 2, free–free). (a) Mode (1, 0) at $r = r_o$, (b) mode (1, 0) at $r = r_i$. Key as Figure 6.

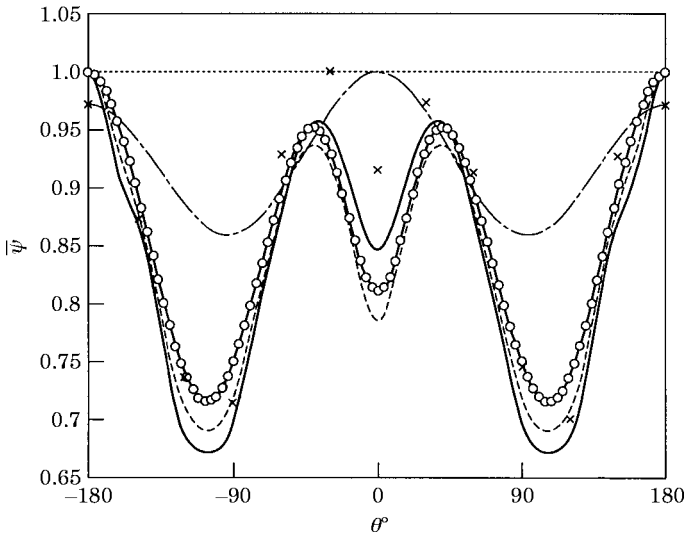

Figure 8. Effect of the number of shape function terms used in the Ritz method on the modal displacements of mode (1, 0) at $r = r_o$ for the annular disk with one hole (case 2, free–free). Key —○—, $N_r = 3$, $N_\theta = 8$; – – – –, $N_r = 3$, $N_\theta = 12$; – · – · –, $N_r = 6$, $N_\theta = 3$; ——, $N_r = 6$, $N_\theta = 12$; ×, experiment; . . . . , case 1 (without any holes).

that an estimation with $N_r = 6$ and $N_\theta = 3$ is poor but other estimations are reasonable and for instance good results are obtained with $N_r = 6$ and $N_\theta = 12$. The mode shape $\Psi_r(r, \theta)$ is expanded in terms of the bi-orthogonal set of equations (11–14) as

$$\psi_r(r, \theta) = \left[\sum_{i=1}^{N_s} \eta_i S_i(r, \theta) \right]_r = \left[\sum_{l=0}^{N_r} \sum_{k=0}^{N_\theta} \eta_{lk} P_l(r) \Theta_k(\theta) \right]_r, \tag{18}$$

where η_i or η_{lk} is the shape function participation factor that may be evaluated as

$$[\eta_i]_r = \frac{\langle \Psi_r^e(r, \theta), S_i(r, \theta) \rangle_{r,\theta}}{\| S_i(r, \theta) \|_{r,\theta}^2} = [\eta_{lk}]_r = \frac{\langle \psi_r^2(r, \theta), P_l(r) \Theta_k(\theta) \rangle_{r,\theta}}{\| P_l(r) \|_r^2 \| \theta_k(\theta) \|_\theta^2}. \tag{19}$$

To estimate the number of N_r and N_θ terms, first conduct an experimental or computational (FEM) modal analysis. By using equation (19), calculate η_i or η_{lk} for all modes of interest

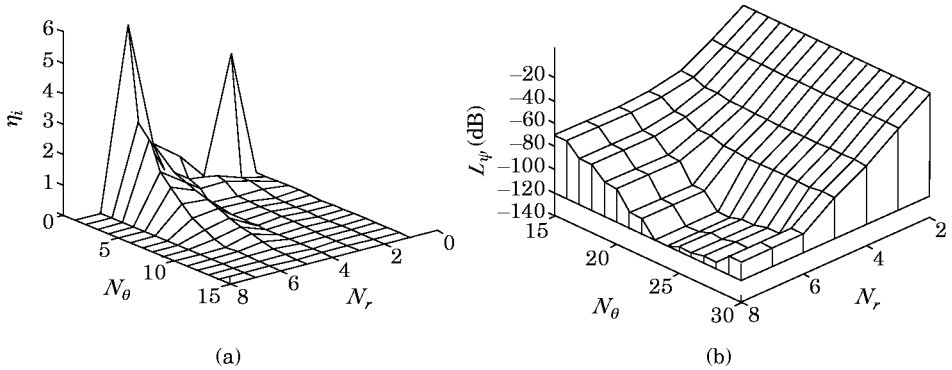

Figure 9. Effect of N_r and N_θ terms on the reconstructed (1, 0) mode of an annular disk with 1 hole (case 2). (a) Shape function participation factor η_i, (b) overall rms error L_ψ.

TABLE 5

Natural frequencies of a free–free annular disk with one annular slot ($\Gamma = -0{\cdot}053$). Refer to Table 1 and Figure 5(b)

Mode		λ^2						
		Case 1 $\Delta r = 10$ *mm*, $\Delta\theta = 0^\circ$	Case 3 $\Delta r = 10$ mm, $\Delta\theta = 129{\cdot}7^\circ$		Case 4 $\Delta r = 20$ mm, $\Delta\theta = 58{\cdot}9^\circ$		Case 5 $\Delta r = 50$ mm, $\Delta\theta = 17{\cdot}5^\circ$	
m, n	r	Expt.	Expt.	FEM	Expt.	FEM	Expt.	FEM
0, 2	1	5·1	4·2	4·2	5·0	4·9	4·8	4·8
	2	5·1	4·9	4·9	5·0	4·9	4·8	4·8
1, 0	3	8·2	6·0	6·0	8·2	7·7	7·8	7·8
0, 3	4	12·2	11·1	11·0	12·1	11·7	11·6	11·7
	5	12·2	11·2	11·2	12·1	11·9	12·2	12·1
1, 1	6	18·6	12·9	12·9	18·8	16·7	17·7	17·9
	7	18·6	16·0	16·2	19·0	18·0	18·2	18·3
0, 4	8	N/A	20·0	20·2	21·4	20·9	20·2	20·6
	9	N/A	20·4	20·5	21·4	21·0	21·3	21·3

N/A = Not measured.

and especially the highest two within the frequency range of interest. Figure 9(a) re-examines Figure 8 in the context of equation (19) where numerical values of η_i are plotted versus N_r and N_θ terms; here the mode shape $\Psi_r^e(r, \theta)$ is known from experimental modal analysis. Observe that participation factors are negligible only when very high numbers of N_r and N_θ terms are used, however the set with $N_r = 6$ and $N_\theta = 12$ appears to be reasonable for this particular mode. A similar analysis can be conducted for other modes.

Yet another estimate is developed by defining the overall root mean square (rms) error L_Ψ, where $\psi_r^e(r, \theta)$ is known from experiment and $\psi_r(r, \theta)$ is obtained from equation (18):

$$L_\psi(N_r, N_\theta) = 10 \log_{10} \left[\frac{\int_{V_B} (\psi_r^e(r, \theta) - \psi_r(r, \theta))^2 \, \mathrm{d}V_B}{V_B^2} \right], \quad \mathrm{d}B. \tag{20}$$

Figure 9(b) illustrates results for L_Ψ versus N_r and N_θ. The conclusions are similar to those observed for the shape function participation factors in Figure 9(a). Note that L_Ψ represents a global error in a spatial modal distribution and a large dynamic range is seen which necessitated the introduction of a logarithmic scale. It is quite different from the Rayleigh's quotient type convergence analyses carried out primarily for the first eigenvalue. Both L_Ψ and η_i definitions can be extended to other dynamic structures as they may be valuable tools in the identification of suitable admissible functions.

6.3. EFFECT OF ONE ANNULAR SLOT (CASES 3–5)

Three annular slot cases (3, 4, 5 with the same mass removal Γ value of $-0{\cdot}053$) are studied for different values of Δr and $\Delta\theta$, and shown in Figure 5(b). Measured and computed (by FEM) eigenvalues are listed in Table 5. Observe that all slots lower the natural frequencies because of mass removal but case 3 produces the biggest change. Some

of the repeated eigenvalues, like case 2 with one circular hole, are split because of the asymmetry produced by an angular slot. The Ritz method is applied to case 3 and the resulting eigenvalues are compared with FEM and experimental data in Table 4 as well as with the results of cases 1 and 2. The annular disk with one annular slot appears to be slightly more compliant than the disk with one circular hole of the same Γ value ($-0{\cdot}053$). Both cases are compared with each other for the (1, 0) mode shape in Figure 10; only measured modal displacements are shown here. We note that modal displacement shapes are quite different. In fact, $\overline{\psi}_r$ for a disk with annular slot depends more on Δr and $\Delta\theta$ values than do the eigenvalues λ_r^2.

6.4. EFFECT OF SEVERAL HOLES (CASES 6–9)

The Ritz method is next applied to annular disks with multiple circular holes (cases 6–9). Table 4 lists eigenvalues for disks with two and three holes each of radius $r_h = 0{\cdot}01998$ m, giving a mass removal ratio $\Gamma = -0{\cdot}105$ and $-0{\cdot}158$, respectively. As expected, natural frequencies shift down as more material is removed. Note that results predicted by the Ritz method are close to those obtained by experiment or FEM.

From the design viewpoint, it may be of interest to find an optimum number of holes or slots for a certain mass removal ratio Γ. Accordingly, experiments were performed on disks with different number of circular holes ($N_H = 2$, 3, 4, and 8) but with the same $\Gamma = -0{\cdot}15$. Results are shown in Table 6 and Figure 11. Observe from Table 6 that λ^2 values of annular-like disks seem to decrease less from the annular plate eigenvalue with an increase in N_H for the same Γ. This shows that in order to obtain the stiffest possible component it might be better to design a disk with many small holes rather than one or a few holes. The second observation is that different numbers of holes within the body split repeated natural frequencies corresponding to different modes. A general rule on frequency splitting based on periodicity consideration can be derived. All circumferential modes with $n = jN_H/2$ if N_H is even or $n = jN_H$ if N_H is odd, where $j = 1, 2, \ldots$, will have

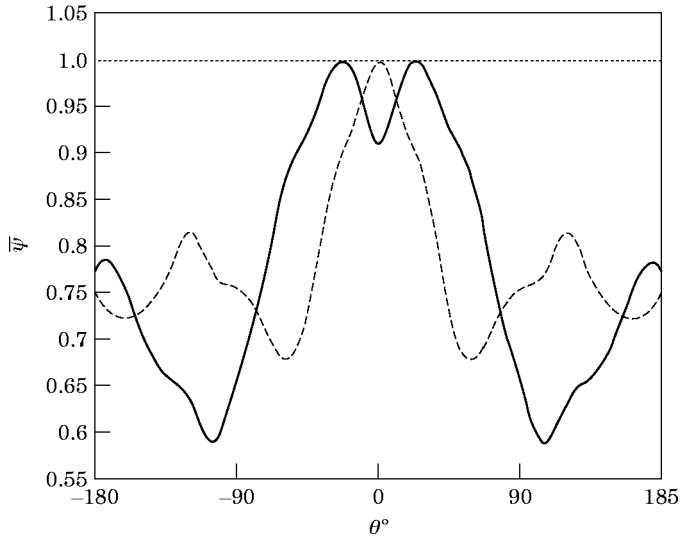

Figure 10. Circular hole (——) vs. annular slot (- - - -) for the (1, 0) mode of the annhular disk (cases 2 and 3, free–free); (· · · ·) case 1. Only measured results are reported here for the same $\Gamma = -0{\cdot}053$.

TABLE 6

Effect of number of holes N_H on the measured natural frequencies of a free–free annular disk. Refer to Figure 5(a) and Table 1

Modes		Experimental λ^2				
m, n	r	$N_H = 0$ (Case 1)	$N_H = 2$ (Case 6)	$N_H = 3$ (Case 7)	$N_H = 4$ (Case 8)	$N_H = 8$ (Case 9)
0, 2	1	5·1	4·5	4·6	4·6	4·7
	2	5·1	4·6	4·6	4·7	4·7
1, 0	3	8·2	7·3	6·9	7·0	7·1
0, 3	4	12·2	11·0	11·0	11·1	11·1
	5	12·2	11·8	11·5	11·1	11·1
1, 1	6	18·6	16·7	16·7	16·6	16·3
	7	18·6	16·7	16·7	16·6	16·3
0, 4	8	N/A	19·5	19·8	19·5	19·5
	9	N/A	20·3	19·8	20·0	19·7

split natural frequencies. Consequently the position of the nodal diameters will be fixed on the disk. Conversely, when the above condition is not satisfied, repeated natural frequencies occur and the nodal diameters can be located anywhere on the annular-like disk like a perfectly symmetric annular plate. This phenomenon has also been reported by Yu and Mote [4] for equally spaced, small radial slots on the plate. Table 6 confirms this rule, where modes $n = 1$, 2 and 3 for $N_H = 2$ holes, $n = 3$ for $N_H = 3$ (case 7), and $n = 2$ for $N_H = 4$ (case 8) exhibit split natural frequencies. Figure 11 shows the measured modal deformation of (1, 0) at $r = r_o$ for these cases. It is obvious that with an increase in the number of circular holes, given the same Γ, this mode of vibration starts to revert back to the shape of an annular plate without any holes even though there are still discontinuities in the body.

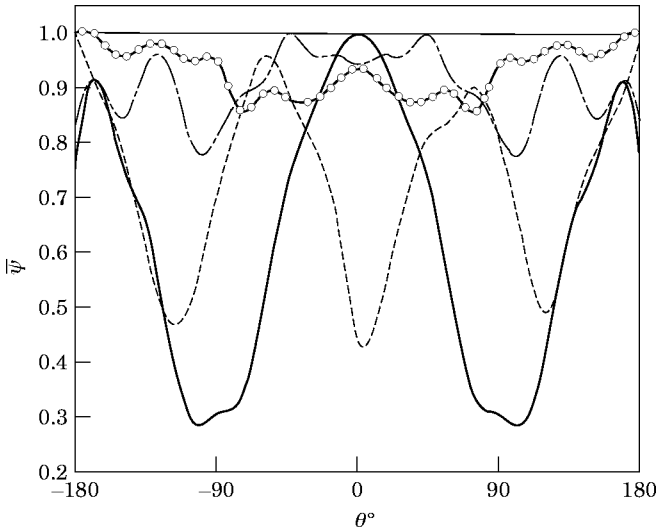

Figure 11. Effect of number of holes (N_H) on the measured (1, 0) mode shapes of the annular disk (cases 1, 6–9; free–free). Key: · · · , $N_H = 0$; ——, $N_H + 2$; – – – –, $N_H = 3$; – · – · – · , $N_H = 4$; —○—, $N_H = 8$.

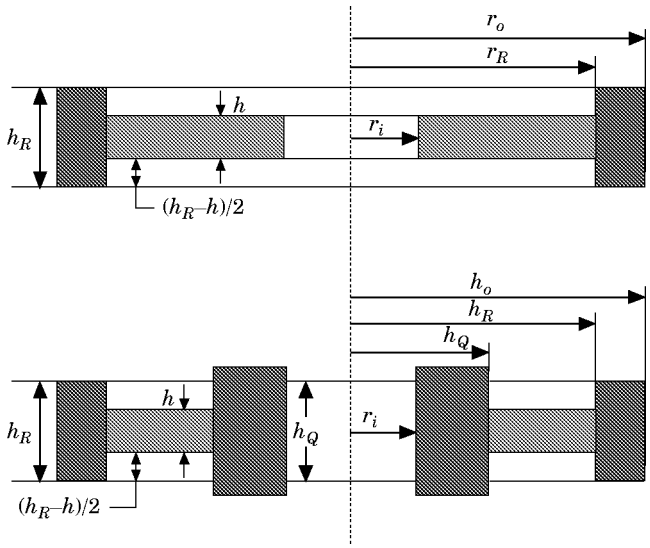

Figure 12. Annular disk with material added without any mechanical joint. (a) Circular ring added at outer rim (case 12), (b) circular ring added at the outer rim and inner hub (case 13).

7. STUDY OF SEVERAL ANNULAR-LIKE DISKS

7.1. DISKS WITH MATERIAL ADDED (CASES 12 AND 13)

The effect of adding material to free–free annular disk without any mechanical attachment was studied by examining a disk with thick rim (of thickness h_R) and hub (of thickness h_Q) regions as shown in Figure 12. For such an annular-like disk, equation (9) can be reduced to the following where subscripts o and i refer to the outer rim and inner hub regions, respectively:

$$\mathbf{K} = \mathbf{K}_B + \mathbf{K}_{A_o} + \mathbf{K}_{A_i}, \qquad \mathbf{M} = \mathbf{M}_B + \mathbf{M}_{A_o} + \mathbf{M}_{A_i}. \tag{21}$$

Table 7 lists the eigenvalues of two cases (12 and 13) as obtained by experiments and the Ritz method. The FEM model was constructed by using 8-noded shell elements with

TABLE 7

Natural frequencies of a free-free annular disk with material added. Refer to Table 1 *and Figure* 12

Mode		Case 11	λ^2					
			Thick Rim (Case 12)			Thick Rim and Hub (Case 13)		
m, n	r	Expt.	Expt.	Ritz	FEM	Expt.	Ritz	FEM
0, 2	1	5·2	6·3	6·5	6·3	7·3	7·3	7·3
	2	5·2	6·5	6·5	6·3	7·3	7·3	7·3
1, 0	3	8·2	9·2	9·4	9·4	10·6	11·2	11·0
0, 3	4	12·6	17·1	17·1	17·1	17·7	17·9	17·7
	5	12·6	17·1	17·1	17·1	17·7	17·9	17·7
1, 1	6	19·3	19·6	20·6	20·2	21·2	22·8	22·0
	7	19·4	19·6	20·6	20·2	21·2	22·8	22·0
0, 4	8	22·3	32·0	32·2	32·0	32·4	32·6	32·4
	9	22·3	32·0	32·2	32·0	32·4	32·6	32·4

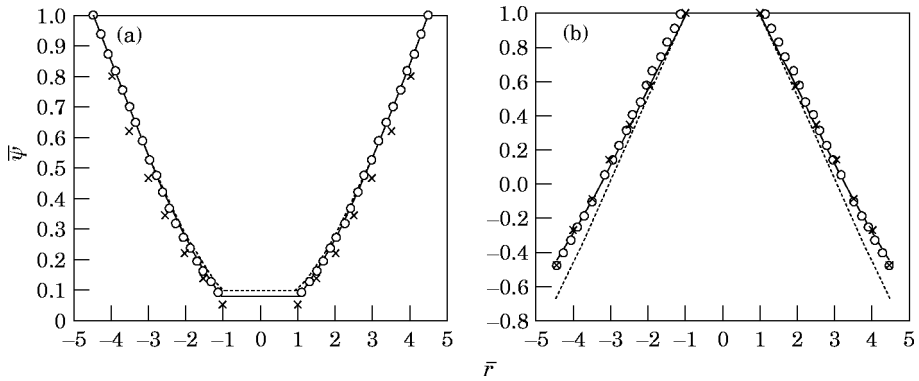

Figure 13. Comparison of mode shapes for the free–free annular disk with material added at the outer rim (case 12). (a) Mode (0, 2) given $\theta = 0{\cdot}0^\circ$, (b) mode (1, 0) given $\theta = 0{\cdot}0^\circ$. Key, $\times$, experimental; $\bigcirc$, FEM; ——, Ritz; · · · ·, mode shape of an annular disk with no material added (case 10).

varying thickness; 390 elements were needed and 100 master-degrees-of-freedom were specified to extract 20 modes. The natural frequencies of an annular disk of thickness 3·175 mm without any material added to rim and hub regions (case 11) are also included in this table for the sake of comparison. The Ritz method based on thin plate theory is successful in predicting results that match well with those from FEM or experiments. Figures 13 and 14 show plots of modal displacements $\bar{\psi}_r(r)$ for modes (0, 2) and (1, 0) of cases 12 and 13, respectively. Observe that there is a very close agreement between the three analysis techniques. Mindlin's thick plate theory was not used for these cases since the thin plate formulation already predicts excellent results.

Table 7 shows that an addition of material to the rim (case 12) with $\Gamma = 0{\cdot}57$ raises the eigenvalues by about 20% over those for the regular disk (case 11). A further increase in the material to the Γ value of 0·603, now at the inner edge (case 13), stiffens the disk by approximately 40% when compared to the annular plate (case 11). From these results it appears that the mass loading effects are substantial. The concept of adding material at the design stage in the form of outer and inner rings is fruitful in obtaining a very stiff disk. From the mode shapes of Figures 13 and 14 we do not observe any discontinuities in displacement near the abrupt changes in thickness from h to h_R or h_Q. Even though the

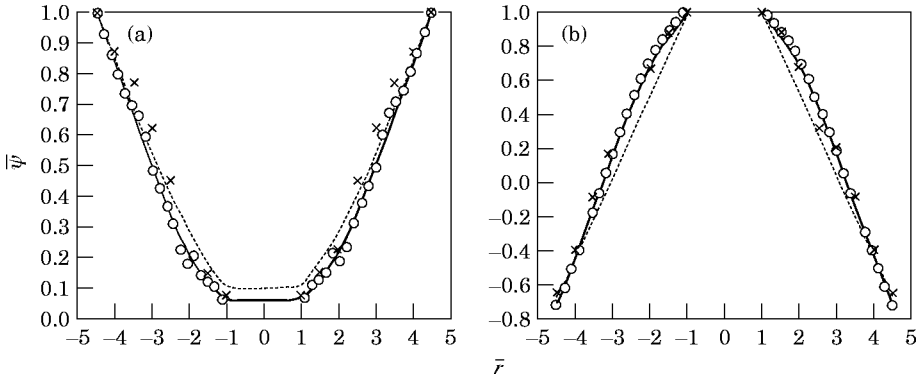

Figure 14. Comparison of mode shapes for the free–free annular disk with material added at the outer rim and inner hub (case 13). (a) Mode (0, 2) given $\theta = 0{\cdot}0^\circ$; (b) mode (1, 0) given $\theta = 0{\cdot}0^\circ$. Key as Figure 13.

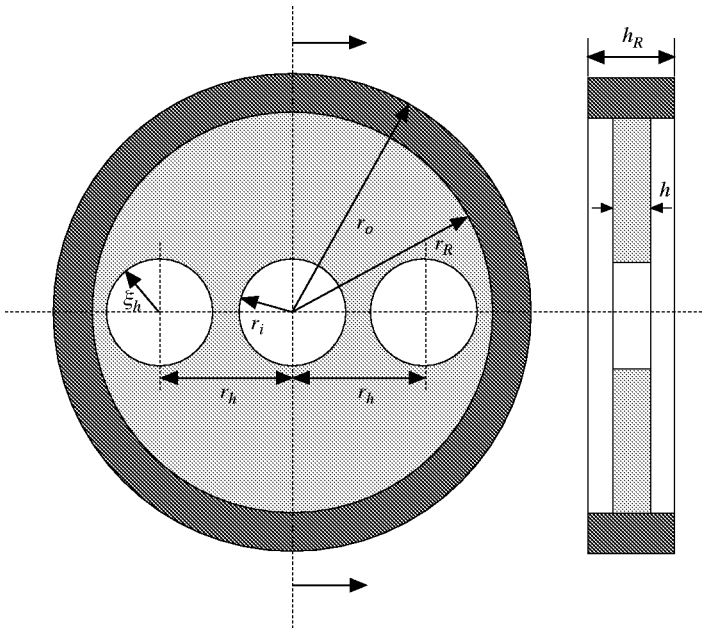

Figure 15. Annular-disk with both material intentionally removed (two identical circular holes) and added (thick outer rim): case 14.

$\overline{\psi}_r(r, \theta)$ shapes seem to be the perturbed forms of the mode shapes of a regular annular plate (case 11) which are also plotted in Figures 13 and 14, significant coupling between modal displacements in radial and circumferential directions has been observed.

7.2. ANNULAR DISK WITH BOTH MATERIAL ADDED AND REMOVED (CASE 14)

Finally an annular-like disk (case 14) was fabricated which had two circular holes and a thick outer rim as shown in Figure 15. This example is conceptually a combination of cases 12 and 6. Starting from the material addition value of $\Gamma = 0{\cdot}576$, an introduction of two holes reduces this to $\Gamma = 0{\cdot}322$. As with the example considered in the previous section, 300 8-noded shell elements with 150 master-degrees-of-freedom were needed to develop a FEM model. Again the thin plate theory was used for the Ritz method based on the results of cases 12 and 13. The experimental modal analysis techniques was used only to extract natural frequencies for both free–free and clamped–free boundary conditions. All results including those for an annular plate (case 11) are listed in Tables 8(a) and (b). The Ritz method is particularly effective in predicting the dynamic behaviour of this composite disk since a discrepancy of 5% or less is seen between measured and computed eigenvalues. Observe from Table 8(a) for the free–free boundaries that this case (14) is significantly more stiff than the regular annular disk (case 11). However, a decrease of about 3 to 9% in natural frequencies is seen when it is compared with case 12 without any holes. Comparable results in Table 8(b) for the clamped–free disk are somewhat mixed. First three eigenvalues of the composite disk (case 14) corresponding to (0, 1) and (0, 0) modes are now lower than those for an annular disk (case 11), and the rest higher. It appears that material removal (holes) controls the first few eigenvalues more effectively than material addition at the outer rim. In fact, both holes are very close to the inner clamped edge. The Ritz results are obtained by using model IV of Figure 3(e) (impedance boundary condition) to simulate the inner clamped boundary.

TABLE 8

Natural frequencies of an annular disk with both material added (thicker rim) and material removed (two holes). Refer to Table 1 and Figure 15

(a) *Free-free*

Mode m, n	r	λ^2 Case 11 Expt.	λ^2 Case 14 Expt.	λ^2 Case 14 Ritz	λ^2 Case 14 FEM
0, 2	1	5·2	6·3	6·1	6·1
	2	5·2	6·3	6·3	6·3
1, 0	3	8·2	9·0	9·0	9·0
0, 3	4	12·6	16·9	16·7	16·7
	5	12·6	16·9	16·9	16·9
1, 1	6	19·3	18·6	19·2	18·3
	7	19·4	22·8	23·2	22·8
0, 4	8	22·3	32·2	31·8	31·6
	9	22·3	32·2	31·8	31·8

(b) *Clamped-free*

Mode m, n	r	λ^2 Case 11 Expt.	λ^2 Case 14 Expt.	λ^2 Case 14 Ritz
0, 1	1	4·3	3·3	3·7
	2	4·3	3·9	4·1
0, 0	3	4·8	4·5	4·7
0, 2	4	6·4	6·9	7·1
	5	6·4	7·3	7·3
0, 3	6	12·9	17·3	17·3
	7	12·9	17·7	17·3

Figure 16. Gear from a helicopter tail rotor gearbox: case 14.

7.3. GEAR FROM HELICOPTER TAIL ROTOR GEAR BOX

As a final confirmation of the proposed Ritz formulation a real life machine element was analyzed. As seen from the photograph of Figure 16 the gear has a thin web, a thick outer rim with teeth, a thick inner hub with internal splines and eight identical circular holes distributed symmetrically within the body. An extensive FEM model with 4900 eight-noded isoparametric tetrahedral elements and 200 master-degrees-of-freedom was needed to successfully predict the eigensolutions for this case; it is shown schematically in Figure 17. A pitch radii of inner splines and outer teeth are used in both FEM and Ritz calculations for r_i and r_o values, respectively. Experiments were confined to impulse testing in the free–free mode and only the first 7 natural frequencies were measured as reported in Table 9. Even a very small accelerometer (0·5 g) did split some of the repeated roots when it was placed at the outer edge because of asymmtry created by mass loading. When the accelerometer was shifted to the inner edge, the difference in repeated roots was less than 1% which could only be measured by the zoom FFT analysis. All eigenvalues of Table 9 have, however, been rounded off to $\pm 0{\cdot}1$ as mentioned before and therefore some of the minor splits in repeated roots can not be observed from this table. Mode shapes were not measured due to insufficient number of locations where compact accelerometers could be placed. The Ritz method is particularly more successful in predicting the eigensolutions than the FEM model as noted by Table 9. Significant savings in computational time are also characteristic of the Ritz method, especially for this example case. Unlike Hayashi *et al*.'s thick plate model of the helical gear-shift system [13, 14], the present analysis is based on thin plate theory. The gear example used is more appropriate

TABLE 9

Natural frequencies of a free-free gear from a helicopter tail rotor gearbox. Refer to Table 1 *and Figures* 16 *and* 17

Mode m, n	r	λ^2 Expt.	Ritz	FEM
0, 2	1	0·8	0·8	0·7
	2	0·8	0·8	0·7
1, 0	3	1·1	1·2	1·1
0, 3	4	1·5	1·6	1·6
	5	1·7	1·7	1·6
0, 4	6	2·4	2·2	2·0
	7	2·4	2·2	2·0

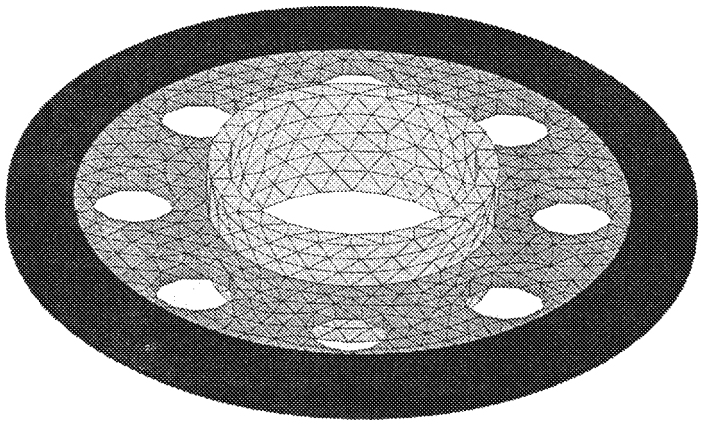

Figure 17. Finite element model of a gear from helicopter tail rotor gearbox: case 15.

for the analytical models developed in this article compared with the helical gear analyzed in references [13, 14], which resembles an annular plate.

8. CONCLUSION

The proposed bi-orthogonal polynomial-trigonometric function basis is particularly effective in describing the eigensolutions of annular-like disks and associated phenomena including strong coupling between radial and circumferential modes and splitting of appropriate repeated roots. The numbers of N_r and N_θ terms used in the shape function matrix are obviously problem specific but guidelines for their systematic determination are given. Even for a disk with discontinuities, smooth modal functions consisting of a combination of linearly independent bases are found in both theory and experiment over the physical domain and, as expected, periodicity consisting of several sinusoids is observed in circumferential direction. The alternate models used to describe the inner edge clamping in experiments illustrate the importance of impedance boundary condition. The concept, in conjunction with the recent articles by D'Angelo and Mote [12], Hayashi *et al*. [13, 14] and Pabst and Hagedorn [25], should aid future researchers in judiciously choosing idealizations for their specific boundaries.

Analytically computed and experimentally measured eigenvalues for a variety of material addition and removal cases should clarify the dynamic behaviour of many real-life annular-like disks. Many of these examples including the gear have not been examined previously in a generic fashion, to the best of our knowledge. As expected, a weak relationship between dynamic properties and the global design parameter (mass removal or addition fraction Γ) was observed because the eigensolutions are governed more by the spatial distribution of holes, slots, rings and the like. The semi-analytical Ritz method has been very successful in predicting first 7 to 9 modes when compared with measured and computed (FEM) results. The Ritz method yields savings over FEM by at least one order of magnitude in terms of computational time excluding detailed efforts that are often needed to construct geometric models of complicated structures with commercial FEM codes. Even more attractive is the ease with which the Ritz method can be integrated in component mode synthesis or multi-body dynamics type techniques which attempt to analyze large scale structures or equipment. The authors are already working along these directions. Impedance boundary models will be used to describe interfaces between a disk and a shaft and at other locations where conjugate machine element pairs are present.

Experiments are also under way to investigate dynamic coupling between plate flexural and ring modes in those annular-like disks where a significantly large amount of material has been removed or added to the blank. Calculations of forced vibration response and sound radiation are also included in future research plans.

ACKNOWLEDGMENT

This research has been supported by the Army Research Office (URI Grant DAAL 03-92-G-0120; 1992-97; Project monitor: Dr T. L. Doligalski).

REFERENCES

1. A. Leissa 1993 *Vibrations of plates*. Acoustical Society of America.
2. S. Y. Lee and S. M. Lin 1979 *Journal of Sound and Vibration* **136**, 425–437. Free vibration of elastically restrained non-uniform plates.
3. P. A. A. Laura, R. O. Grossi and G. I. Carnerio 1979 *Journal of Sound and Vibration* **63**, 499–505. Transverse vibration of rectangular plates with thickness varying in two directions and with edges elastically restrained against rotation.
4. R. C. Yu and C. D. Mote, Jr 1987 *Journal of Sound and Vibration* **119**, 409–427. Vibration and parametric excitation in asymmetric circular plates under moving loads.
5. I. Y. Shen and C. D. Mote, Jr. 1992 *Journal of Sound and Vibration* **155**, 443–465. Dynamic analysis containing small elastic imperfections: theory with application to asymmetric plates.
6. S. Kitipornachai, Y. Xiang and K. M. Liew 1994 *Journal of Sound and Vibration* **173**, 457–470. Vibration analysis of corner supported Mindlin plates of arbitrary shape using the Lagrange multiplier method.
7. K. M. Liew, Y. Xiang, S. Kitipornchai and C. M. Wang 1994 *Journal of Sound and Vibration* **177**, 689–707. Buckling and vibration of annular Mindlin plates with internal concentric ring supports subject to in-plane radial pressure.
8. K. M. Liew 1992 *International Journal of Mechanical Science* **34**, 511–520. Frequency solutions for circular plates with internal supports and discontinuous boundaries.
9. B. Singh and S. Chakarverty 1994 *Journal of Sound and Vibration* **173**, 289–299. Use of characteristic orthogonal polynomials in two dimensions for transverse vibration of elliptic and circular plates with variable thickness.
10. X. Wang, A. G. Striz and C. W. Bert 1993 *Journal of Sound and Vibration* **164**, 173–175. Free vibration analysis of annular plates by the DQ method.
11. H. Larrondo, V. Topalian, D. R. Avalos and P. A. A. Laura 1994 *Journal of Sound and Vibration* **177**, 137–139. Comments on ''Free vibration analysis of annular plates by the DQ method''.
12. C. D'Angelo and C. D. Mote, Jr. 1993 *Journal of Sound and Vibration* **168**, 1–4. Natural frequencies of a thin disk, clamped by thick collars with friction at the contacting surfaces at high rotating speed.
13. I. Hayashi, N. Iwatsuki and H. Maki 1994 *Journal of Sound and Vibration* **173**, 633–655. The theoretical modal analysis of a circular plate with a solid shaft.
14. I. Hayashi, N. Iwatsuki and H. Maki 1994 *Journal of Sound and Vibration* **173**, 657–682. The estimation and measurement of the sound power radiated from a circular plate with a solid shaft subjected to an axial load.
15. K. M. Liew, C. W. Lim and M. K. Lim 1994 *Journal of Sound and Vibration* **177**, 479–501. Transverse vibration of trapezoidal plates on variable thickness– unsymmetric trapezoids.
16. C. M. Wang and V. Thevendran 1993 *Journal of Sound and Vibration* **163**, 137–149. Vibration analysis of annular plates with concentric supports using a variant of Rayleigh–Ritz method.
17. R. D. Mindlin 1951 *Transactions of American Society of Mechanical Engineers*, *Journal of Applied Mechanics* **18**, 31–38. Influence of rotatory inertia and shear on flexural motions of isotropic elastic plates.
18. R. D. Mindlin and H. Dereshowitz 1954 *Journal of Applied Physics*, **25**, 1329–1332. Thickness-shear and flexural vibrations of a circular disk.

19. E. F. Ayoub and A. W. Leissa 1990 *Transactions of American Society of Mechanical Engineers, Journal of Applied Mechanics*, **57**, 995–999. Free vibration and tension buckling of circular plates with diametral point forces.
20. M. R. Lee and R. Singh 1994 *Journal of Acoustical Society of America* **95**, 3311–3323. Analytical formulations for annular disk sound radiation using structural modes.
21. U. Kristiansen and W. Soedel 1971 *Journal of Engineering for Industry, Transactions of the ASME* **93**, 343–345. Fundamental frequencies of cutout square plates with clamped edges.
22. A. Achong 1995 *Journal of Sound and Vibration* **183**, 157–168. Vibrational analysis of circular and elliptical plates carrying point and ring masses and with edges elastically restrained.
23. G. M. Oosterhout, P. J. M. van der Hoogt and R. M. E. Spierling 1995 *Journal of Sound and Vibration* **183**, 33–47. Accurate calculation methods for natural frequencies of plates with special attention to higher modes.
24. K. M. Liew, S. Kitipornchai and Y. Xiang 1995 *Journal of Sound and Vibration* **183**, 401–419. Vibration of annular section Mindlin plates with internal radial line and circumferential arc supports.
25. U. Pabst and P. Hagendorn 1995 *Journal of Sound and Vibration* **182**, 565–575. Identification of boundary conditions as a part of model correction.
26. ANSYS, ver. 5·0, 1993 Swanson Analysis Systems Inc., Houston, PA.

APPENDIX A: LIST OF SYMBOLS

$\mathscr{D}$	differential operator matrix
$\mathbf{E}$	elasticity matrix
f, g, i, j, k, l, p, q	indices
f_r	natural frequencies
h	disk thickness
$\mathbf{I}$	identity matrix
k, $\mathbf{K}$	stiffness and stiffness matrix
L	overall rms error in mode shape
m, $\mathbf{M}$	mass and mass matrix
m	modal index in the radial direction (r)
N	number of terms or holes
n	modal index in the circumferential direction (θ)
$\mathscr{P}$	polynomial shape function
$\mathbf{q}$	generalized coordinate vector
$\mathscr{R}$	subspace
r, θ, z	cylindrical coordinates
$\mathbf{r}$	transverse displacement vector
r	radius or modal index
$\bar{r}$	dimensionless radius (r/r_o)
S, $\mathbf{S}$	shape function and shape function matrix
T	kinetic energy
U	potential Energy
V	volume
Γ	material removal or addition fraction
η	shape function participation factor
λ^2	eigenvalue parameter (dimensionless)
ν	poisson's ratio
Θ	trigonometric shape function
ρ	density
σ	boundary condition
ω	natural frequency (rad/s)
ξ	radius of circular holes
$\psi, \overline{\psi}$	mode shape and normalized modal displacement

Subscripts

A	material addition
B	blank
c	outer edge of clamp
H	material removal (holes, slots, etc.)
i	inner
f, g, k, l, m, n, p, q	indices
o	outer
Q	hub
r	modal index
R	rim
S	shape function
σ	boundary condition